JOURNAL OF MATERIALS SCIENCE 30 (1995) 938–951

Yttria-stabilized hafnia-zirconia thermal barrier coatings: the influence of hafnia addition on TBC structure and high-temperature behaviour

H. IBÉGAZÈNE, S. ALPÉRINE, C. DIOT
ONERA Materials Science Department, B.P. 72, 92322 Châtillon cedex, France

The search for more reliable and durable thermal barrier systems is a key factor for future aircraft turbine engines success. Hafnia is therefore an attractive ceramic component due to its similarity to zirconia and its elevated structural transformation temperatures. We report here structural and thermomechanical investigations of various plasma-sprayed coatings composed of $ZrO_2 + x$ mol % HfO_2 ($x = 0$, 25, 50 and 100), partially stabilized by 4.53 mol % yttria. X-ray diffraction studies show that, a metastable, non-transformable, high yttrium content, tetragonal solid solution is the only phase observed on the as-sprayed samples. This phase is crystallographically equivalent to the t′ phase described for classical yttrium-partially stabilized zirconia (Y-PSZ) thermal barrier coatings (TBCs). Upon high-temperature annealing in air ($T = 1200\,^{\circ}C$), however, the return of this t′ phase to equilibrium differs from the classical $t' \rightarrow t + c$ reaction. According to literature data, reactions of the type $t' \rightarrow t + c + m$ should prevail at the highest hafnia contents ($x \geqslant 50$). Indeed, important quantities of monoclinic phase are accordingly being observed upon cooling. Thermal cycling of TBC samples in air has been performed at 1100 °C. The Young's modulus of the ceramic coating, which progressively increases when hafnia is substituted for zirconia, has a strong influence on TBC thermomechanical resistance.

1. Introduction

Thermal barrier coatings (TBC) have been commonly used over the past 20 years to increase the durability of gas turbine engine combustors working in the 650–750 °C temperature range. The use of TBC to increase turbine engine efficiency, which implies coating high-temperature components (vanes and blades), is still a technical challenge [1]. For this purpose, the state of the art consists of an MCrAlY bond coat about 100 μm thick covered by a 200–300 μm thick ZrO_2–8 wt % Y_2O_3 top coat (this composition is equivalent to 4.5 mol % Y_2O_3 and 9 mol % $YO_{1.5}$). Both can be plasma sprayed (low-pressure plasma spray (LPPS) for the bond coat and air plasma sprayed (APS) for the ceramic [2, 3]) or deposited by an electron beam physical vapour deposition process [4, 5].

A major problem to solve in TBCs is that of the coatings' thermomechanical resistance at elevated temperature (typically 1100 °C and above). Many authors have shown that this property is closely related to the phase structure of the ceramic part of the coating [6–8]. In the 6–8 wt % Y_2O_3 composition range, a non-equilibrium tetragonal t′ phase is retained at room temperature, because of rapid quenching during plasma spraying [9, 10]. This t′ phase displays particular faulted microstructural features, such as grain twinning and antiphase boundaries [11, 12]. Moreover, after high-temperature annealing in air (1100–1200 °C), a very fine and stable precipitation of the equilibrium cubic phase appears ("tweed" microstructure). It has been pointed out that these microstructural elements, absent outside this composition range, would act as crack deviation sites and thus enhance coating intrinsic toughness.

In practice, however, the use of zirconia-based TBC seems limited to a temperature well below 1200 °C for several reasons, one of which is the lack of perenniality of the ceramic microstructure. The aim of this study was to select and examine a new oxide system that would exhibit microstructures similar to that of zirconia and transform at higher temperatures. The current knowledge on the hafnia–zirconia system is reported in the following section. We have attempted to shed some light upon the influence of hafnia addition on the microstructure and high-temperature behaviour of plasma-sprayed yttrium-partially stabilised zirconia (Y-PSZ) coatings. For this purpose, such coatings have been observed by conventional scanning and transmission electron microscopy as well as X-ray diffraction. Particular attention has been paid to the defects structures of the observed tetragonal phase, compared to that of the metastable t′ phase of plasma-sprayed ZrO_2–8 wt % Y_2O_3. The influence of high-temperature annealing on the microstructure has also been studied, giving some insights on how it evolves toward equilibrium in these new coatings. Finally, a qualitative approach of the thermomechanical

0022–2461

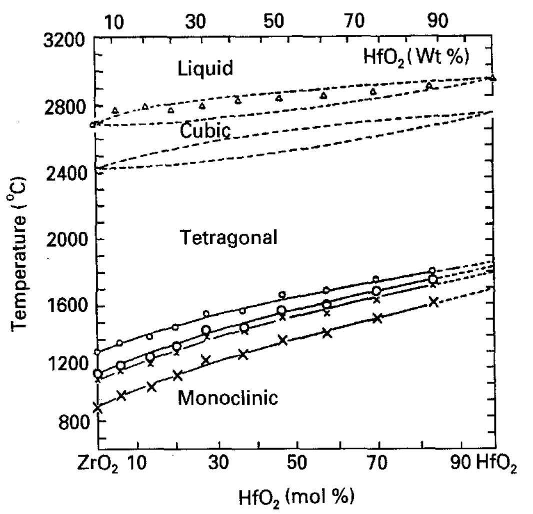

Figure 1 ZrO_2–HfO_2 phase diagram [17].

resistance of the coatings has been developed using thermal cycling and Young's modulus measurements.

2. The ZrO2-HfO2 system

Hafnium and zirconium are both elements of the IVB group. Their ionic radii are very similar: 0.086 nm for Zr^{4+} and 0.085 nm for Hf^{4+} with the eight-fold coordinence (cubic and tetragonal polymorphs of zirconia and hafnia, for instance) [13]. Their respective oxides are therefore, characterized by remarkable structural and chemical similarities. Hafnia and zirconia have very comparable thermal expansion coefficients, close to $10 \times 10^{-6} K^{-1}$ for their tetragonal polymorph [14]. Moreover, the volume change associated with the tetragonal to monoclinic transition is about twice as small in hafnia than it is in zirconia [15]. Hafnia is, therefore, more thermal shock resistant, but less adequate as transformation toughening agent [16].

The zirconia–hafnia binary phase diagram established by Ruh *et al.* [17] is presented in Fig. 1. It reveals that these oxides are miscible in all proportions and at all temperatures. At normal atmospheric pressure, hafnia and zirconia exist in three stable forms: monoclinic, tetragonal and cubic. Table I summarizes some crystallographic data available on ZrO_2 and HfO_2 polymorphs. The transition between these phases occurs at much higher temperatures (see Table II) as the composition moves from ZrO_2 to HfO_2 [17]. Moreover, Lefêvre [18] claims that HfO_2 is probably the only oxide the dissolution of which induces a rise in the transformation temperatures of zirconia. Owing to its important technological application (transformation toughening mechanism), the tetragonal to monoclinic inversion has been the most extensively studied. Its transition temperature could not be measured with great accuracy because of the martensitic character of the transformation and its hysteresis (about 100 °C for ZrO_2 and 30 °C for HfO_2, after Wolten [19]).

However, to prevent this destructive transformation, hafnia like zirconia can be stabilized transformed as a cubic structure, by addition of CaO, MgO, or Y_2O_3. This structure is commonly called "fully stabilized HfO_2 or ZrO_2" or "fluorite-type phase". It has been shown [20] that Y_2O_3-stabilized HfO_2 is more resistant to destabilization at high temperatures than either CaO- or MgO-stabilized HfO_2. According to Stubican and Hannon [21], the hafnia–yttria system phase diagram presents the same features as the zirconia–yttria system (Fig. 2). A remarkable fact is that the 4.5 mol % Y_2O_3 composition line approximately intersects the middle area of the (t + c) phase field in both yttria partially stabilized zirconia and hafnia. Thus, interest in the ZrO_2–HfO_2–Y_2O_3 systems arises from its potential to develop favourable microstructural features and behave mechanically as ZrO_2–8 wt % Y_2O_3.

3. Experimental procedure

The substrates used were $25 \times 50 \times 3$ mm^3 platelets and cylinders (diameter 15 mm, height 36 mm) of cast alloy Ni–23Co–20Cr–8.5Al–4Ta, wt % (this composition matches that of the AMDRY 997, without yttrium), which were grit-blasted (Al_2O_3 220 mesh, 2 bar) and degreased (vapour-phase trichloroethylene). The substrates were first coated with a 100 µm thick NiCoCrAlTaY bondcoat deposited by low-pressure plasma spraying (from Ni–23Co–20Cr–8.5Al–4Ta–0.6Y wt %, AMDRY 997 powder). The MCrAlY bondcoat is required to confer adequate oxidation resistance and to minimize the stresses associated with the thermal expansion mismatch between the ceramic

TABLE I Summary of crystallographic data of ZrO_2 and HfO_2

	Monoclinic		Tetragonal			cubic	
	$P2_1/c$ (no. 0.14)		$P4_2/nmc$ (no. 0.137)	Pseudo-cubic cell		$Fm3m$ (no. 0.225)	
	ZrO_2	HfO_2	ZrO_2	ZrO_2 (at 1020 °C)	HfO_2 (at 1865 °C)	ZrO_2	HfO_2 (at 2750 °C)
Cell parameters (nm)	$a = 0.51463$ $b = 0.52135$ $c = 0.53110$ $\beta = 99.2°$	$a = 0.51156$ $b = 0.51722$ $c = 0.52948$ $\beta = 99.18°$	$a = 0.364$ $c = 0.527$	$a = 0.512$ $c = 0.525$	$a = 0.514$ $c = 0.525$	$a = 0.509$	$a = 0.530$
References	ASTM 36–420	[40]	[27]	ASTM 17–923	ASTM 8–342	ASTM (27–997)	[41]

TABLE II Transformation temperatures (°C) for zirconia and hafnia (after [39]); the first numbers indicate the beginning of the transformation; the numbers between brackets show tranformation completion temperatures

	M⇄T	T⇄M	T⇄C	C⇄Liq.
ZrO_2	1050 (1110)	910 (804)	2370	2680
	1160 (1215)	1038 (993)		
HfO_2	1540 (1650)	1590 (1510)	2520	2753
	1620 (1650)	1620 (1520)	2530	2774
	1725		2660	2800
			2700	2900

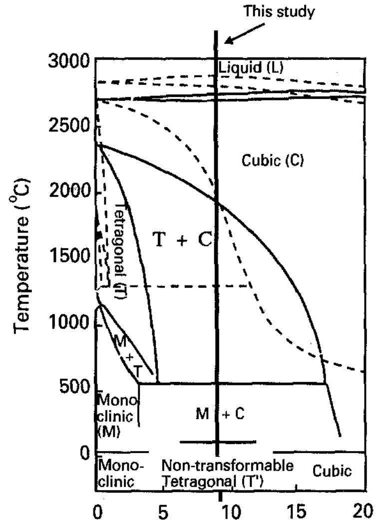

Figure 2 Zirconia–yttria [22] and (...) hafnia–yttria [21] phase diagrams.

and the substrate. The composition of the substrate was chosen in order to minimize bondcoat/substrate interdiffusion. The samples were then heat treated for 4 h at 1080 °C under secondary vacuum ($P_{tot} < 10^{-5}$ torr; 1 torr = 133.322 Pa) for bondcoat diffusion and finally covered with a 300 μm thick layer of [ZrO_2–$x$$HfO_2$]–4.5 mol % Y_2O_3 ($x = 0$, 25, 50 and 100 mol %). The ceramic was air plasma sprayed starting from ZIRCYT powders (mean diameter is around 30 μm). Table III shows the composition of each sample. The 4.5 mol % of added yttria corresponds to a stabilization state equivalent to that of the classical ZrO_2–8 wt % Y_2O_3. Plasma-spraying parameters are listed in Table IV. Isothermal annealing of the specimens was performed at 1200 or 1400 °C in a tubular furnace, in air, for 100 h, followed by an air quench. Thermal cycling was carried out at 1100 °C in two tubular furnaces fitted out with an automatic device. Two cylinder samples per range of composition were cycled to insure the test's validity. Two different cycling experiments have been performed. One involves a 1 h dwelling time and combines the effect of thermal shocks with that of high-temperature oxidation. The other provides a very short stay at 1100 °C, and simulates thermomechanical degradation in less-oxidizing conditions.

The different steps of a cycle are as follows (see also Fig. 3):

(i)	sample introduction:	6 min
(ii)	upward temperature gradient:	17 min
(iii)	isothermal annealing at 1100 °C (± 5 °C):	60 or 1 min
(iv)	sample withdrawal:	5 s
(v)	sample cool-down with forced air convection:	4 min to 200 °C
(vi)	total cycle duration:	87 or 28 min

Young's modulus has been determined by a pulse-echo overlap technique on as-sprayed, 100 h at 1200 °C and 100 h at 1400 °C annealed samples. This method enables calculation of the velocity of propagating longitudinal ultrasonic waves in the material. The knowledge of wave velocity, V_L, leads to the Young's modulus of the coating via the following expression

$$E = \rho V_L^2 \tag{1}$$

where ρ is the specific weight of the material. The samples used are 50 × 5 × 0.3 mm^3 strips. The preparation involves precutting of the ceramic strips, followed by a dissolution (60% concentrated HCl, 20% acetic acid and 20% hydrogen peroxide) of the underlying metallic alloys.

X-ray diffraction data were obtained using a Philips PW 1380 Omega goniometer under the conditions listed in Table V. The {1 1 1} and {4 0 0} regions of the diffraction patterns were extensively analysed. Lattice parameters of the tetragonal phase, measured by X-ray diffraction (XRD), provided indirect value of the percentage of yttria in the tetragonal phase. The following expressions, derived from the experimental work by Scott [22], link a_t and c_t parameters to the molar per cent of $YO_{1.5}$(ξ)

$$a_t\,(\mathrm{nm}) = 0.508 + 3.58 \times 10^{-4}\,\xi \tag{2}$$

$$c_t\,(\mathrm{nm}) = 0.5195 - 3.1 \times 10^{-4}\,\xi \tag{3}$$

TABLE III Chemical composition (mol %) of the raw powders in the zirconia–hafnia–yttria system

Samples (raw powders)	ZrO_2 (%)		HfO_2 (%)		Y_2O_3 (%)	
	Nominal	Observed	Nominal	Observed	Nominal	Observed
ZrO_2–Y_2O_3	95.47	92.65	–	–	4.53	4.54
ZrO_2–25HfO_2–Y_2O_3	71.60	68.78	23.87	24.07	4.53	4.51
ZrO_2–50HfO_2–Y_2O_3	47.73	46.08	47.73	47.10	4.53	4.49
HfO_2–Y_2O_3	–	–	95.47	94.29	4.53	4.53

TABLE IV Air plasma spray parameters

Parameter	Value
Argon flow	$28.3\,\mathrm{l\,min^{-1}}$
H_2 flow	$8\,\mathrm{l\,min^{-1}}$
Arc current	500 A
Powder flow	$18\,\mathrm{g\,min^{-1}}$
Spray distance	110 mm
Torch displacement velocity	$20\,\mathrm{m\,min^{-1}}$

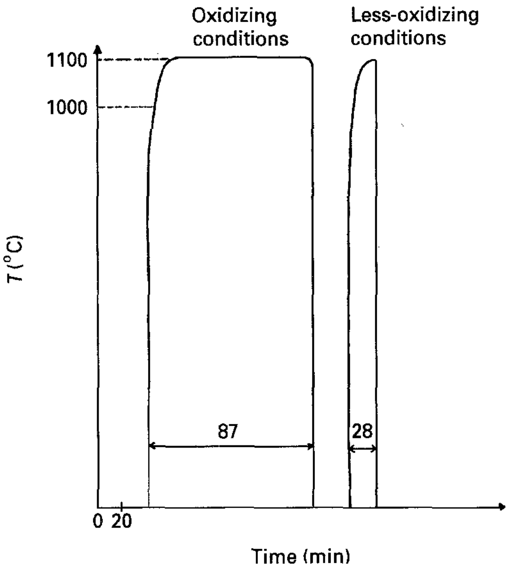

Figure 3 Temperature–time profile for the two thermal cycling conditions.

TABLE V X-ray diffraction instrumental parameters

Radiation	Cu K_α
Postspecimen-type curved graphite monochromator	
{1 1 1} peaks	
Range (2θ)	27°–33°
Step	0.01°
Counting time per step	60 s
{4 0 0} peaks	
Range (2θ)	72°–76°
Steps	0.02°
Counting time per step	120 s

Thus

$$\xi(\%) = \left[\frac{0.5195 - (0.508\,c_t/a_t)}{3.1 + (3.58\,c_t/a_t)}\right] 10^4 \tag{4}$$

It should be noted that the validity of these expressions is supposedly limited to the ZrO_2–Y_2O_3 system. Equivalent data for the HfO_2–Y_2O_3 are not available.

Quantitative analysis of monoclinic phase (concerning both tetragonal and cubic phase) in ZrO_2–50 mol % HfO_2–4.5 mol % Y_2O_3 and HfO_2–4.5 mol % Y_2O_3 samples, annealed 100 h at 1200 °C, is approximated by considering the low-angle X-ray diffraction data in the $27° \leqslant 2\theta \leqslant 33°$ angular region. The size range of the grains (0.1–1 μm) is well below the 5 μm size required for accurate intensities measurement by powder XRD [23] and there is no preferential orientation. This {1 1 1} region corresponds to the most intense reflections of monoclinic, tetragonal and cubic phases. In the case of the diffractometer used in this study, the intensity $I(hkl)$ of (hkl) reflections can be calculated from [24]

$$I(h\,k\,l) = K_0 \frac{p}{\mu}\left(\frac{1 + \cos^2 2\theta \cos^2 2\theta_M}{\sin\theta\ \sin 2\theta}\right)\frac{|F_{hkl}|^2}{U^2}\, e^{-2M} \tag{5}$$

where K_0 is a constant, p the multiplicity of planes (hkl), μ the linear absorption coefficient of the material, θ the Bragg angle, θ_M the monochromator crystal Bragg angle, $F(hkl)$ the structure factor, e^{-2M} the Debye–Waller temperature factor, and U the crystallographic unit cell volume. The $\cos^2\theta_M$ factor is introduced for the Lorentz–Polarization correction for a post-specimen type monochromator.

Equation 5 can also be written as

$$I(hkl) = K_0 \frac{R(hkl)}{\mu} \tag{6}$$

Following Toraya *et al.* [23], the volume fraction, V_m, of the monoclinic phase in pure zirconia (m + t) mixtures is calculated from

$$V_m = \frac{PX_m}{1 + (P-1)X_m} \tag{7}$$

where

$$P = \frac{R_t(1\,0\,1)}{R_m(\bar{1}\,1\,1) + R_m(1\,1\,1)} \tag{8}$$

The values of R_m are calculated with atomic parameters of monoclinic ZrO_2 given by Smith and Newkirk [25], lattice parameters of Adams and Rodgers [26] and R_t with all correct crystallographic parameters of Teufer [27]. Toraya *et al.* [23] obtained a theoretical value of $P = 1.34$. The experimental value of $P = 1.311$ resulting from X-ray diffraction measurements on 19 samples is in agreement with the theoretical value.

X_m, the integrated intensity ratio, is defined for this mixture by

$$X_m = \frac{I_m(\bar{1}\,1\,1) + I_m(1\,1\,1)}{I_m(\bar{1}\,1\,1) + I_m(1\,1\,1) + I_t(1\,0\,1)} \tag{9}$$

The (1 0 1) reflection of the tetragonal primitive cell [27] corresponds, in the pseudo cubic cell, to the (1 1 1) reflection habitually used.

In addition, Toraya *et al.* [28] have also studied the quantitative analysis of monoclinic-stabilized cubic ZrO_2 system by X-ray diffraction. Indeed, they consider that the equation for the non-linear calibration curve of volume fraction versus integrated intensity ratio are still valid in the case of (m + c) mixtures. In this system, the integrated intensity ratio is defined as

$$X_m = \frac{I_m(\bar{1}\,1\,1) + I_m(1\,1\,1)}{I_m(\bar{1}\,1\,1) + I_m(1\,1\,1) + I_c(1\,1\,1)} \tag{10}$$

TABLE VI Crystallographic data used for quantitative phase analysis (by [40] for monoclinic phase, [27] for tetragonal phase, ASTM 27-997 for cubic ZrO_2, and Pearson [2] for cubic HfO_2)

(a) Cell parameters

	Monoclinic	Tetragonal	Cubic
ZrO_2	$a =$ 5.1454 $b =$ 5.2075 $c =$ 5.3107 $\beta = 99.23°$	$a =$ 3.64 $c =$ 5.27	$a =$ 5.09
HfO_2	$a =$ 5.1156 $b =$ 5.1722 $c =$ 5.2948 $\beta = 99.18°$	$a =$ 3.64 $c =$ 5.27	$a =$ 5.125

(b) Atoms coordinates for monoclinic cells
(after the data by [25] for ZrO_2 and by [40] for HfO_2)

ZrO_2	x	y	z	B
Zr	0.2758	0.0411	0.2082	0.30
O_I	0.0700	0.3360	0.3410	0.32
O_{II}	0.4420	0.7550	0.4790	0.23
HfO_2				
Hf	0.2759	0.0412	0.2078	0.45
O_I	0.0730	0.3460	0.332	0.45
O_{II}	0.4460	0.7480	0.4880	0.45

and

$$V_m = \frac{P X_m}{1 + (P - 1) X_m} \tag{11}$$

where V_m is the volume fraction of monoclinic ZrO_2.

For our study, the qualitative analysis of the monoclinic phase by X-ray diffraction is not problematic. On the other hand, a tentative approximation of monoclinic volume fraction in ZrO_2–HfO_2–Y_2O_3 system is more critical because the calculation or experimental evaluation of P could not be very accurate, owing to the lack of adequate crystallographic data. However, based on the data given in Table VI, theoretical calculations of $R(h\,k\,l)$ for monoclinic and tetragonal polymorphs of ZrO_2 and HfO_2 have been performed (see Table VII). Substituting these results in Equation 8, the following P values for pure zirconia and hafnia were obtained using, respectively $(1\,0\,1)_t$ and $(1\,1\,1)_c$ reflections

$$P(\mathrm{m/t\text{-}ZrO_2}) = 1.267 \qquad P(\mathrm{m/c\text{-}ZrO_2}) = 1.347$$

$$P(\mathrm{m/t\text{-}HfO_2}) = 1.229 \qquad P(\mathrm{m/c\text{-}HfO_2}) = 1.314$$

In view of these results and the dispersion of P values found in the literature, an average value of $P = 1.30$ has been retained for the estimate of V_m. The integrated intensities of monoclinic and tetragonal (or cubic) peaks were evaluated by area measurements considering a linear adjustment of the background level.

The preparation of transverse samples for scanning electron microscopy involved four steps: sample embedding in epoxy resin or electrolytic nickel, crosswise sectioning, mechanical thinning and conductive carbon deposit. Surface imaging was done using a Cambridge Stereoscan S250 SEM.

Electron-transparent thin foils for TEM have been prepared from planar sections of coating, using the following steps. The ceramic topcoat was first removed by chemical etching of the substrate and the bond coat (60% concentrated HCl, 20% acetic acid and 20% hydrogen peroxide). It was then mechanically prethinned (to ~ 70 μm) and ion milled (Ion Tech. Supermicrolap Mark 2) at an incident angle of 17° until perforation occurred. They were studied using conventional transmission electron microscopy with Philips CM 20, JEOL 200CX and JEOL 4000 FX microscopes.

4. Results

4.1. Microstructure of as-sprayed and annealed samples

4.1.1 As sprayed specimens

4.1.1.1. X-ray analysis. X-ray diffraction (XRD) analyses of as-sprayed samples show, for each composition ratio, the presence of a single tetragonal phase. Indeed, in these materials, the monoclinic form is

TABLE VII Theoretically calculated X-ray diffraction data for ZrO_2 and HfO_2 polymorphs

Material	Reflection	$d\,h\,k\,l$ (nm)	2θ (°)	$LP(\theta)$	p	U (10^{-3} nm³)	$\lvert F\rvert^2$	R
Cubic ZrO_2	(1 1 1)	0.2938	30.39	12.03	8	131.87	16615	91.95
Tetragonal ZrO_2	(1 0 1)	0.2995	29.81	12.54	8	69.82	4199	86.41
Monoclinic ZrO_2	$(1\,1\,\bar{1})$	0.3162	28.19	14.10	4	140.45	13971	39.94
Monoclinic ZrO_2	(1 1 1)	0.2838	31.49	11.16	4	140.45	12476	28.23
Cubic HfO_2	(1 1 1)	0.2958	30.18	12.21	8	134.61	51030	275.2
Tetragonal HfO_2	(1 0 1)	0.2995	29.81	12.54	8	69.82	12499	257.2
Monoclinic HfO_2	$(1\,1\,\bar{1})$	0.3145	28.35	13.93	4	138.30	39720	115.7
Monoclinic HfO_2	(1 1 1)	0.2825	31.64	11.05	4	138.30	40481	93.54

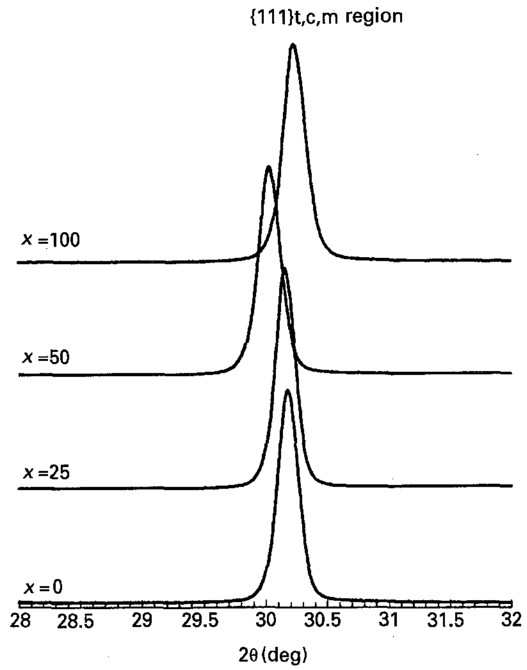

Figure 4 XRD patterns of plasma-sprayed ZrO_2–x mol % HfO_2–4.5 mol % Y_2O_3. Detail of the {1 1 1} region for $x = 0, 25, 50$ and 100.

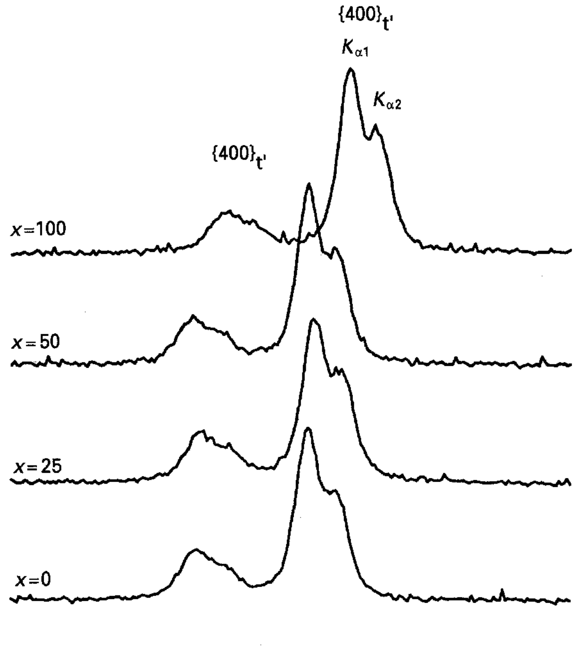

Figure 5 XRD patterns of plasma-sprayed ZrO_2–x mol % HfO_2–4.5 mol % Y_2O_3. Detail of the {0 0 4} region for $x = 0, 25, 50$ and 100.

TABLE VIII X-ray diffraction results of as-sprayed samples

Samples	a_t (nm) (± 0.0001)	c_t (nm) (± 0.0001)	c_t/a_t (± 0.0002)
ZrO_2–Y_2O_3	0.5111	0.5159	1.0093
ZrO_2–25HfO_2–Y_2O_3	0.5110	0.5157	1.0091
ZrO_2–50HfO_2–Y_2O_3	0.5112	0.5161	1.0095
HfO_2–Y_2O_3	0.5094	0.5145	1.0100

distinguished from the cubic and the tetragonal (t and t′) forms through the observation of the $\{1\,1\,1\}_{m,t}$ reflection (the pseudo-cubic description of the tetragonal phase is used here for convenience). On the other hand, c, t and t′ can be differentiated by the separation of $\{4\,0\,0\}_c$, $\{4\,0\,0\}_{t,t'}$ and $\{0\,0\,4\}_{t,t'}$ reflections at higher 2θ angles.

Partial X-ray diagrams in the {1 1 1} region are shown for each sample in Fig. 4. The examination of this region shows the presence of the intense (1 1 1) reflection of the tetragonal (or cubic) phase and very weak {1 1 1} reflections of the monoclinic phase (not visible on the figure). Some amount of monoclinic phase is also detected whatever the hafnia content. However, calculations based on peak heights above the background level and Equations 5–9 lead us to consider this amount to be less than 2% (volume fraction) for all samples.

The equivalent X-ray diffraction patterns from the {4 0 0} region are shown in Fig. 5. The presence of two peaks in this region is characteristic of t or t′ tetragonal phases.

From the lattice parameter ratios reported in Table VIII, the corresponding values of ξ were calculated using Scott's formulae [22] (Table IX). For $x = 0$, 25 and 50 the high Y_2O_3 content of the tetragonal phase, derived from Equations 2–4, and c/a ratio close to unity, suggest the presence of the metastable t′ phase. For $x = 100$, agreement with high yttria content (i.e. 4.5 mol % Y_2O_3) is only obtained on the basis of c/a evaluation (see Equation 4). This fact is not surprising considering the validity domain of Scott's formula [22] and the slight difference between Zr^{4+} and Hf^{4+} ionic radii.

It should be noted that, although the observed diffraction peaks lead to the conclusion that all coatings are composed of a single non-equilibrium t′ phase, low amounts of the equilibrium c and t phases could be present and undetected because their reflections in the {0 0 4} region lie in the same angle range as those of t′. To check for this eventuality, XRD measurements have been performed on mechanically ground samples. The mechanical energy thus provided would probably transform any amount of t phase back into its low-temperature stable monoclinic form [29]. Fig. 6 shows the related X-ray diffractograms of such samples in the $\{1\,1\,1\}_{m,t}$ region. Compared to the equivalent diffractogram of as-sprayed samples, no transformation seems to have occurred during grinding, because the observed ratio $I_m/(I_m + I_t)$ has not markedly change. The observed tetragonal phase is accordingly a non-transformable t′ phase.

4.1.1.2. *Ceramic microstructure.*

Fig. 7 illustrates the typical aspect of the cross-section of thermal barrier coatings. The coatings exhibit a morphology of lamellar drops and a relatively important and uniform amount of porosity. Backscattered electron imaging also shows a heavily microcracked structure.

Fig. 8 shows, for all compositions, a microstructure of fine equiaxed grains in the size range 0.1–1 μm. Some grains sometimes are slightly elongated. The fine characterization of the microstructure is achieved

TABLE IX Compositions for t′ metastable tetragonal phase derived from crystallographic data of Table VIII

Samples	ξa (mol % $YO_{1.5}$) ± 0.5	ξc (mol % $YO_{1.5}$) ± 0.5	$\xi c/a$ (mol % $YO_{1.5}$) ± 1
ZrO_2–Y_2O_3	8.8	11.4	10.0
ZrO_2–25HfO_2–Y_2O_3	8.3	12.1	10.1
ZrO_2–50HfO_2–Y_2O_3	9.0	10.8	9.9
HfO_2–Y_2O_3	4.1	15.9	9.3

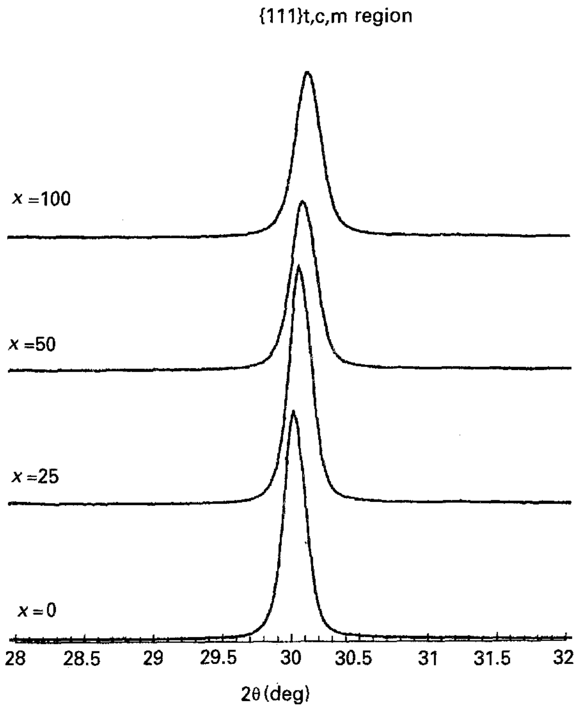

Figure 6 XRD patterns of ground plasma-sprayed ZrO_2–x mol % HfO_2–4.5 mol % Y_2O_3. Detail of the {1 1 1} region for x = 0, 25, 50 and 100.

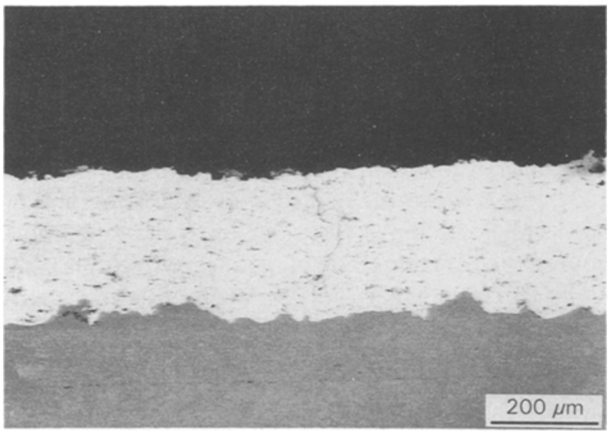

Figure 7 Typical aspect of the cross-section of a TBC top layer; SEM backscattered electron image.

by using dark-field imaging technique. Indeed, the tetragonality of the coating is revealed in experimental diffraction mode by the presence of weak reflections (forbidden for the F Bravais lattice) of the type {odd, odd, even} (with the relevant index permutations). Using these reflections, the appearance of

Figure 8 (a), (b) and (c) (see over)

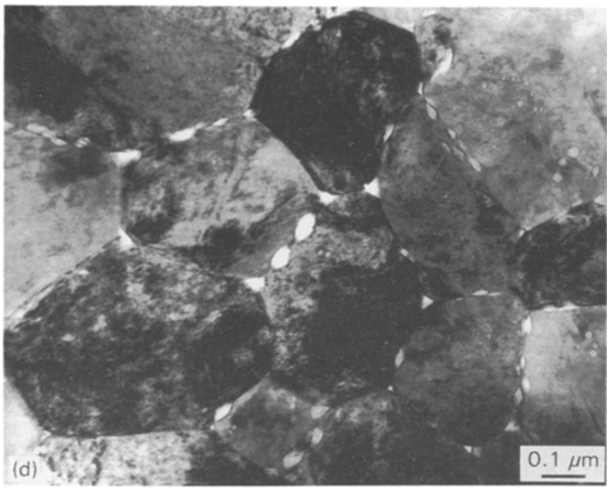

Figure 8 TEM bright-field image of planar sections showing equiaxed grains for x = (a) 0, (b) 25, (c) 50 and (d) 100. Porosity lines are seen in some instances.

grain twinning and domains structure (tetragonal variants separated by anti-phase boundaries, APBs) inside each diffracting twin is always displayed (see Fig. 9). At a subgrain level the observed tetragonal phase also exhibits microstructural features similar to the well-studied t′ phase in ZrO_2–6 to 8 wt % Y_2O_3 [30, 31].

These microstructural features (domain microstructure and APBs inside the twins) result from the decrease of symmetry during the c → t′ displacive transformation [11]. Twin microstructure occurs because of the equivalent possibility for the tetragonal distortion to be along any of the three original ⟨1 0 0⟩ axes of the parent cubic cells.

4.1.2. Annealed specimens

4.1.2.1. X-ray analysis. Partial X-ray diagrams for annealed samples in the {1 1 1} and {0 0 4} regions have been performed. The observation of XRD diagrams leads us to consider separately low ($x = 0, 25$) and high ($x = 50, 100$) hafnia content specimens.

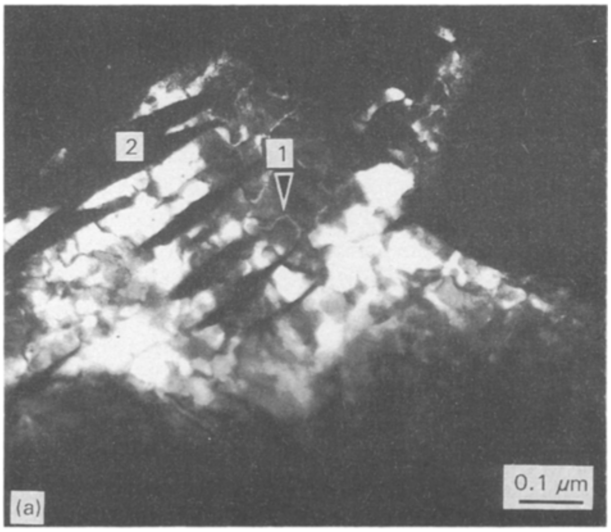

Figure 9 (a)

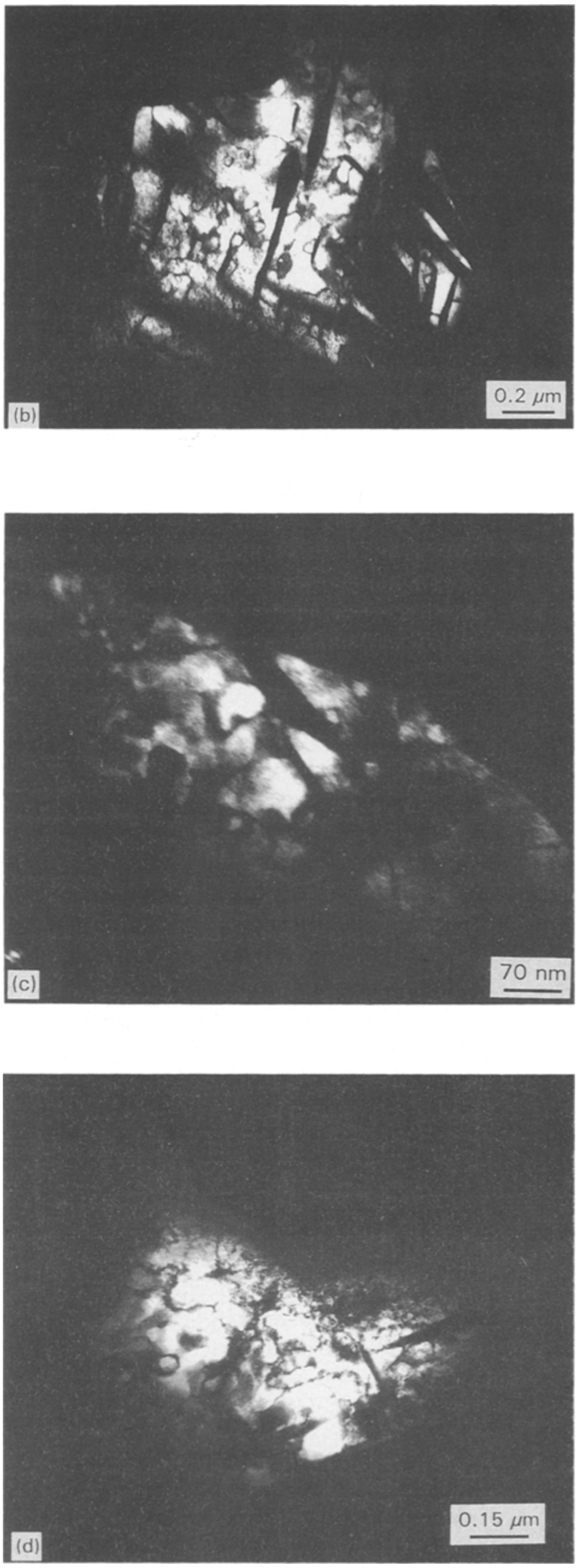

Figure 9 (a–d) TEM dark-field image of tetragonal t′ grain with ⟨1 1 1⟩ zone axis; $g = \{1\,1\,2\}$; (1) APB, (2) extinguished twin; x = (a) 0, (b) 25, (c) 50 and (d) 100.

Fig. 10 shows the {1 1 1} region diffractograms for the low hafnia content samples. No phase evolution in this region can be observed: the amount of monoclinic is of the same order as in as-sprayed samples. The exploitation of XRD data (see Table X) in the {0 0 4}

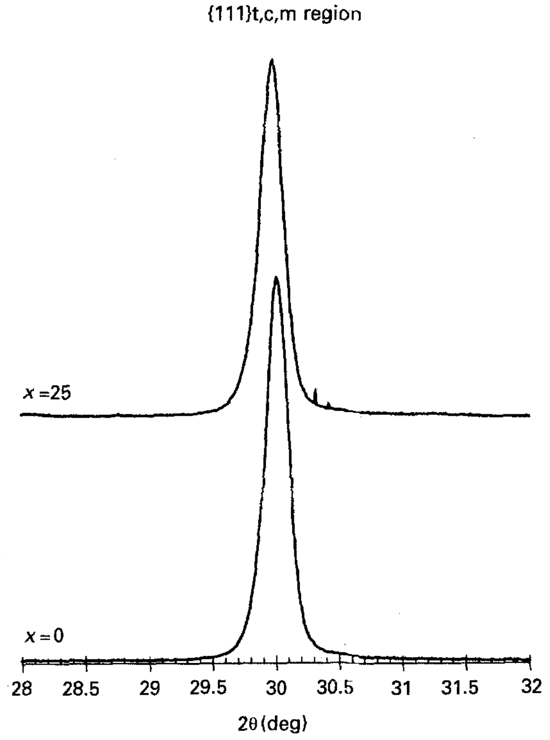

Figure 10 XRD patterns of plasma-sprayed ZrO_2–x mol % HfO_2–4.5 mol % Y_2O_3 annealed 100 h at 1200 °C. Detail of the {1 1 1} region for $x = 0$ and 25.

region shows an increase of the tetragonal c/a ratio and concurrently a weak decrease of the derived $YO_{1.5}$ content ξ (see Table X). These results first reveal that the tetragonal t′ phase is still preponderant after annealing, whereas the yttria content remains high. Moreover, they suggest the development of a second phase, probably with a higher yttria content than t′.

Concerning the higher hafnia content samples the tetragonal to monoclinic transformation is markedly observed in the {1 1 1} region. The increase of the amount of monoclinic phase (see Fig. 11) with increasing hafnia content thereby proves high-temperature destabilization of the non-equilibrium t′ phase. Quantitative estimate of the monoclinic volume fraction, V_m, is achieved by using Equations 5–8. Starting from the value of $P = 1.30$, the calculated amounts of monoclinic phase are $V_m = 68\%$ for HfO_2–Y_2O_3 and $V_m = 16\%$ for ZrO_2–$50HfO_2$–Y_2O_3. Because of this important amount of monoclinic phase, the {0 0 4} region cannot be used in practice because many monoclinic reflections lie in this angular domain.

4.1.2.2. Ceramic microstructure. As has been shown above, phase evolution during annealing differs for samples with low and high hafnia contents. In the first case, the same microstructural features (twins, APBs) are still present after isothermal ageing. The APB boundaries have straightened: this is a classical ripening phenomenon leading to a minimal energy configuration. However, a microstructural change has occurred, consisting of fine regularly spaced dark and bright precipitates (Fig. 12). This feature, commonly called modulated or tweed-like microstructure, has already been observed by several authors [11, 32] in the ZrO_2–Y_2O_3 system annealed in the c + t field. Electron diffraction patterns performed in the {1 1 0} orientation show the presence of reflections forbidden for fluorite structure. It is likely that these precipitates are composed of the equilibrium cubic phase which appears in the t′ matrix as a consequence of solid-state diffusion [31]. This phase evolution can thus be interpreted as an early stage of the return path to equilibrium of the t′ phase.

TEM investigation on ZrO_2–$50HfO_2$–Y_2O_3 ($x = 50$) shows two typical second-phase morphologies. The first predominant one is similar to that developed in low hafnia content samples, namely a tweed pattern structure consisting of cubic precipitates in tetragonal matrix (see Fig. 13a). In other respects, limited numbers of t grains partially transformed into monoclinic phase, are observed. Fig. 13b shows the formation of m laths nucleated at t grain boundaries. Distorted fringe contrast is evinced at the m/t interface. It probably results from the parameter misfit between t and m phases and the volume expansion accompanying the t → m transformation. Other localized strained zones are also evinced when growing m laths impinge on other propagating laths.

In the case of HfO_2–Y_2O_3 samples ($x = 100$), a wide development of monoclinic phase has taken place during isothermal annealing. Fig. 13c shows a heavily transformed region made up of wedge-shaped m plates that are coarsely twinned. In regions transformed to a lesser degree (Fig. 13d), propagating and coarsening m laths are best observed. Localized strained zones are also present but no occurrence of microcracks is evinced at monoclinic/tetragonal grain-boundary interfaces.

4.2. Thermomechanical properties

4.2.1. Thermal cycling

The number of cycles to failure, for individual samples and the two cycling conditions, is plotted versus hafnia content in Fig. 14. This evaluation has been made on the basis of complete spallation of the coating. It should be emphasized that for each composition, failure occurred almost simultaneously for the two samples tested, insuring the test reproducibility. These results clearly show a marked decrease of the samples' lifetime with increasing hafnia content. Moreover,

TABLE X X-ray diffraction results and derived compositions of samples annealed 100 h at 1200 °C

Sample	a_t (nm) ± 0.001	c_t (nm) ± 0.001	c/a ± 0.002	ξ_t(%) ± 1
ZrO_2–Y_2O_3	0.5117	0.5171	1.010	8.34
ZrO_2–$25HfO_2$–Y_2O_3	0.5113	0.5171	1.011	8.79

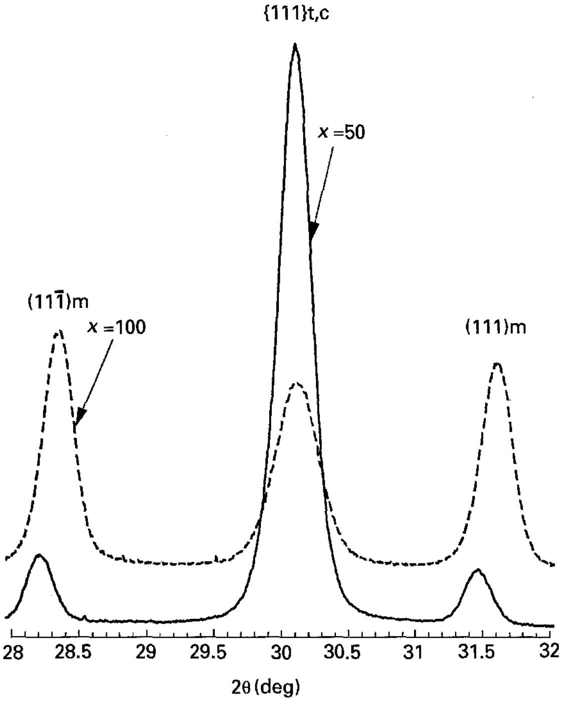

Figure 11 XRD patterns of plasma-sprayed ZrO_2–x mol % HfO_2–4.5 mol % Y_2O_3 annealed 100 h at 1200 °C. Detail of the {1 1 1} region for $x = 50$ and 100.

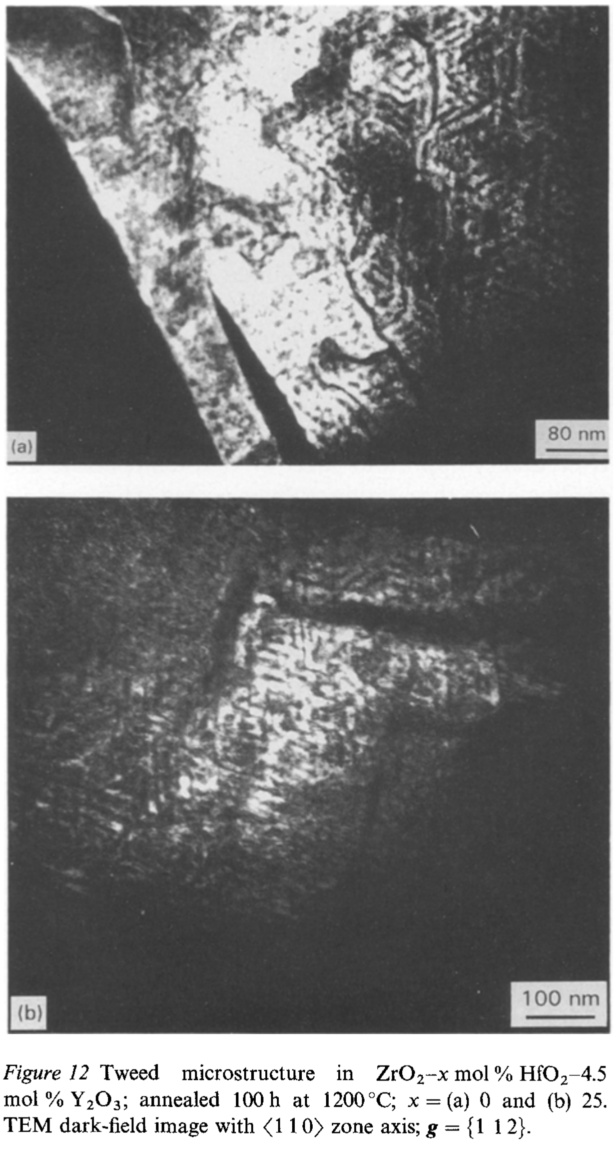

Figure 12 Tweed microstructure in ZrO_2–x mol % HfO_2–4.5 mol % Y_2O_3; annealed 100 h at 1200 °C; x = (a) 0 and (b) 25. TEM dark-field image with ⟨1 1 0⟩ zone axis; $\boldsymbol{g} = \{1\ 1\ 2\}$.

a critical influence of oxidation is evinced because 1 h annealing during thermal cycling leads to specimen lives which are three times shorter.

As has often been observed on plasma-sprayed TBCs [33], the major thermomechanical degradation mode of the samples consists of oxide spallation resulting from progressive accumulation of fatigue damage. A macrocrack usually propagates in the ceramic, parallel to the ceramic/metal interface (Fig. 15).

A thin alumina layer (about 5 μm thick) has grown between the ceramic and the MCrAlY bondcoat. This layer is formed by interaction of aluminium, which has

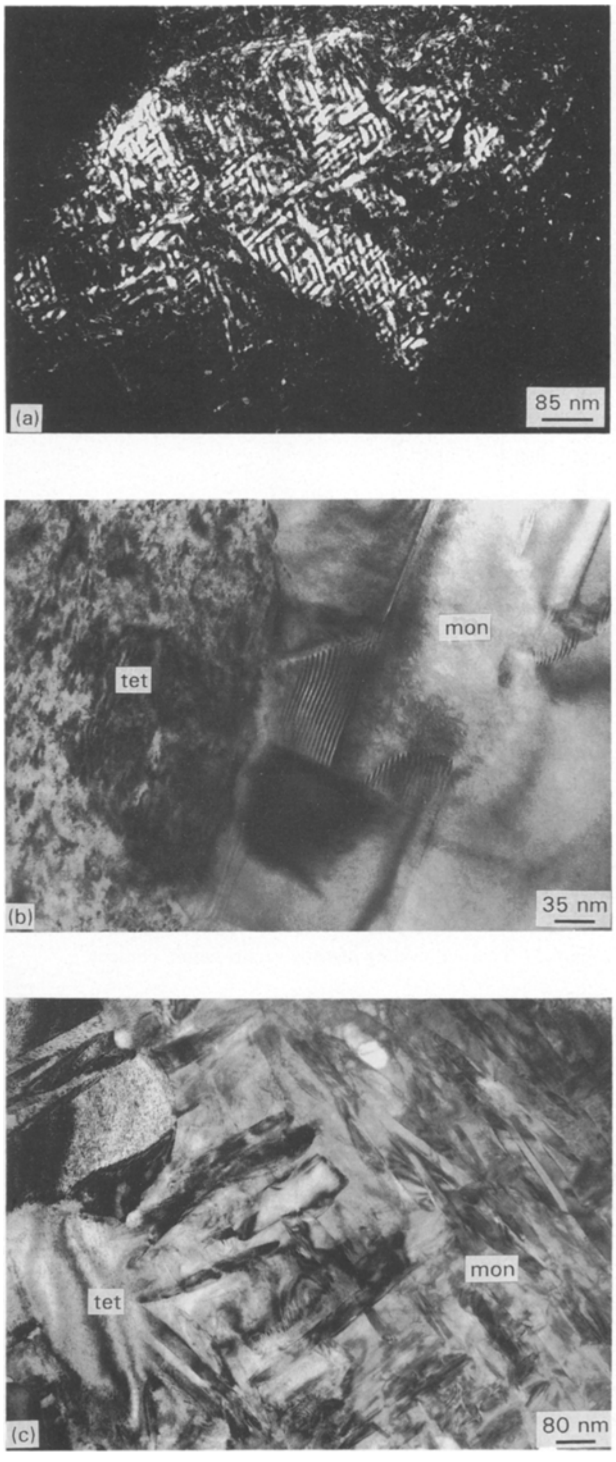

Figure 13 (a), (b) and (c)

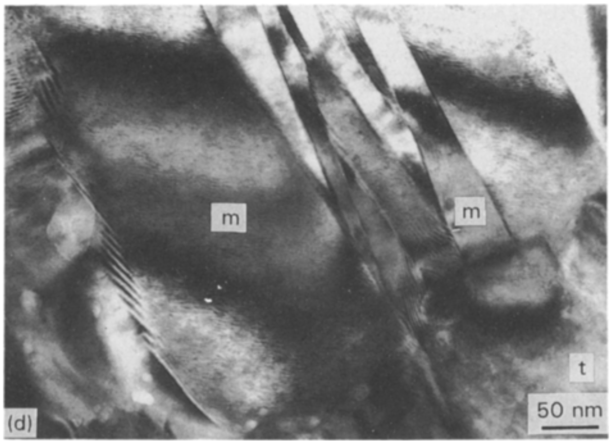

Figure 13 Microstructure of ZrO_2–x mol % HfO_2–4.5 mol % Y_2O_3 annealed 100 h at 1200 °C for x = (a, b) 50 and (c, d) 100; (a) tweed microstructure, (b) growth of m laths nucleated at t grain boundary, (c) extensively transformed region, and (d) details of propagating and coarsening m laths.

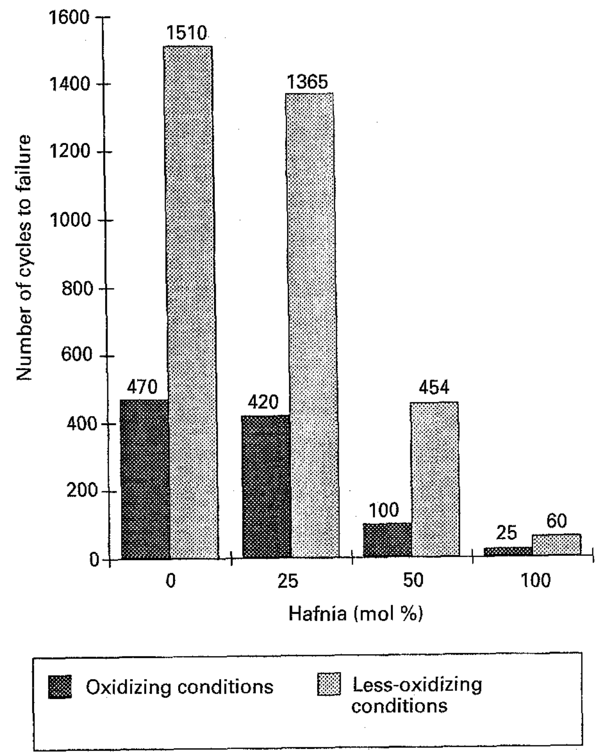

Figure 14 Thermal cycling lifetime versus hafnia content.

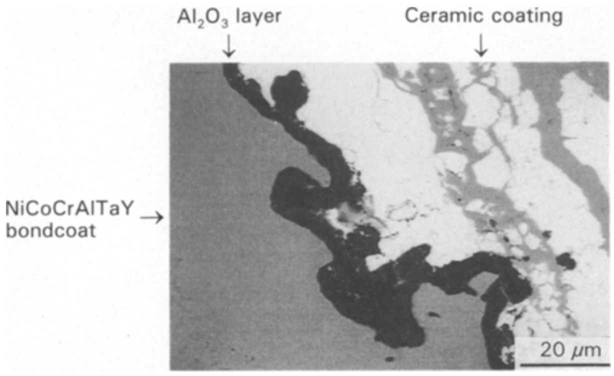

Figure 15 Propagation of a macrocrack near the ZrO_2–x mol % HfO_2–4.5 mol % Y_2O_3/NiCoCrAlTa Y interface during thermal cycling; SEM backscattered electron image; cross-section observation.

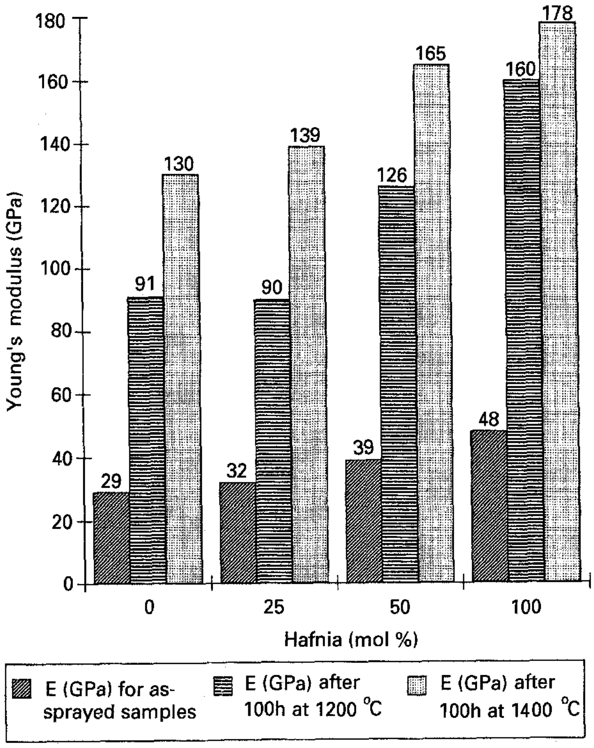

Figure 16 Young's modulus of as-sprayed and annealed samples versus hafnia content.

diffused from the bondcoat, with oxygen present in the oxide coating. It can be very rippled in some right sides. Occurrence of other oxides such as Cr_2O_3 and $Ni(Al, Cr)_xO_y$ is also observed.

4.2.2. Young's modulus

The results of Young's modulus measurements are reported in Fig. 16. The specific weight takes into account a porosity of 10% for each composition (this value for the porosity is recommended by the manufacturer of the coating). On this basis, a significant increase of E versus hafnia content is observed. Moreover, a very important effect of high-temperature annealing upon the coating stiffness is seen. These results are clearly to be correlated with the thermal cycling behaviour of the ceramics.

5. Discussion

5.1. As-sprayed coatings

Generally speaking, the phase composition and microstructure of (ZrO_2–x mol % HfO_2)–Y_2O_3 coatings are in good agreement with our expectations. It has been shown unambiguously that all coatings are composed of a single tetragonal phase. This phase is the equivalent of the so-called t′ phase [30] in the Y-PSZ systems, because:

(i) its yttrium content (4.53 mol %) lies well above the solubility limit of Y_2O_3 in t phase;

(ii) the measured c/a ratios only slightly depart from unity (less than 1%, to be compared with the c/a of about 1.03 in the transformable equilibrium t phase);

(iii) it does not transform into monoclinic, even when mechanical energy is being supplied (ground coatings).

In this regard, the similarities of the Hf^{4+} and Zr^{4+} cations lead to the formation of identical metastable phases during rapid quenching.

From a microstructural point of view, twinning of the t′ grains and pseudoantiphase boundary planes have been observed bearing great similarities with those previously reported by Lelait *et al.* [11] in pure yttria partially stabilized zirconia coatings.

5.2. High-temperature annealing of coatings

Although striking similarities have been observed between the phase and microstructures of ZrO_2–x mol % HfO_2 coatings and their pure zirconia counterparts, the evolution of the microstructures during 1200 °C annealing differs, according to the ceramic hafnia content.

5.2.1. Origin and stability of the tweed microstructure

In ZrO_2–4.5 mol % Y_2O_3 system, the tweed microstructure that develops during intermediate temperature annealing in the c + t field (typically between 1100 and 1300 °C), and consequently leads to solid state diffusion, is believed to be the first step towards the return of the t′ phase to equilibrium [34]. In this very peculiar microstructure, partial decomposition of yttrium had occurred between very small precipitates of cubic phase (somewhat richer in yttrium), arranged on a pseudo-periodic three-dimensional lattice, and the yttrium-depleted tetragonal matrix. One of the most striking features exhibited by this tweed microstructure is the absence of coarsening of the precipitates during long term exposure to temperatures up to 1200 °C [11]. It looks just as if yttrium diffusion and consecutive precipitates classical ripening, had been blocked, soon after the appearance of the cubic precipitates.

According to Perovic *et al.* [35], who have investigated from a mechanical standpoint the possibility of such semi-ordered precipitation, two conditions are necessary for the formation of such arrays of precipitates. First, the included phase should be present with such a volume fraction that the interparticle spacing is of the same order of magnitude as the precipitates typical dimensions. Second, the inclusions should individually give rise to tetragonal distortions within the parent phase (which implies, in practice, cubic precipitation in a tetragonal matrix, or the reverse). Indeed, defects or precipitates giving rise to such a tetragonal distortion can interact quite strongly [36]. Wen *et al.* [37] have developed an energetic model that simulates the reconfiguration of an arbitrary distribution of tetragonal (or cubic) precipitates in a cubic (or tetragonal) crystal. It appears that the elastic interaction between the precipitates tends to stabilize the arrays of precipitates against the Ostwald ripening phenomenon. The importance of this elastic field is that it couples with the composition field and thus influences the coarsening behaviour of the precipitates [38]. Perovic *et al.* [35] also showed the possibility to obtain stabilization of arrays of precipitates facing competitive growth processes.

The analysis quoted above is very much relevant to the case of the tweed precipitates in the tetragonal matrix. On the one hand, high-temperature annealing tends to allow yttrium diffusion and t′ decomposition. The driving force that leads to this reaction is the metastability of the t′ phase at this temperature. On the other hand, the strong elastic interaction between the cubic nuclei (or very small precipitates) and the depleted matrix opposes further precipitate growth, and thus further decomposition. As long as the specific energies involved in these two contradictory phenomena are of the same order of magnitude, there will be a critical size of the precipitates that will not be exceeded (the cost in terms of increase in elastic energy being too high). Conversely, it is logical to think that if the annealing temperature is being raised, the corresponding increase in the specific energy associated to yttrium diffusion would allow the precipitates to grow further to a size where higher elastic energy would again counter that of yttrium diffusion.

Now, if the two specific energies mentioned above are not of the same order of magnitude, two situations can be observed:

(i) if the energy associated with yttrium diffusion is the lower, the t′ phase remains stable and no precipitation occurs (this is the case in YPSZ annealed below 1100 °C);

(ii) if, on the contrary, this energy is the higher, the critical precipitate size diverges and the system completely returns to equilibrium (this is the case for YPSZ annealed above 1300 °C).

5.2.2 Hafnia-containing samples

It has been quoted above that when hafnia is progressively substituted for zirconia the main phase transformation temperatures are accordingly shifted upwards. Few bibliographic data concerning the solid state c → t′ transformation that appears during plasma spraying, are available. Lelait [31] has performed high-temperature X-ray measurements on ZrO_2–8 wt % Y_2O_3 plasma-sprayed samples which showed that this transformation was reversible and took place between 1400 and 1500 °C on cooling. It is reasonable to assume that this temperature should also be shifted upwards with increasing hafnia contents.

If one considers again the idea of the driving force for yttrium diffusion and return of the t′ phase to equilibrium, it is logical to think that, at a given temperature, this driving force should be all the more powerful that the t′ phase is far from equilibrium. It is also logical to assume that t′ is all the more unstable because it is far from its c → t′ transformation temperature. Thus, we can assume that at a given temperature (1200 °C, for instance) the driving force associated with yttrium diffusion becomes higher when hafnia is substituted for zirconia.

This idea accounts, to a reasonable extent, for the differences observed in the microstructure of the various annealed samples. For $x = 25$, no significant microstructural change (compared to $x = 0$) has been observed. For $x = 50$, it has been observed that some t′ grains have been depleted in yttrium to such an extent that the $t \rightarrow m$ transformation has occurred (which would not appear for $x = 0$ until 1400 °C [34]); this means that the diffusion-specific energy locally overrides that of precipitates/matrix elastic interaction. The case of Y_2O_3 stabilized pure hafnia ($x = 100$), illustrates this evolution well, because most of the coating has transformed back into the equilibrium phases and the tweed microstructure is here definitely unstable.

This last case somewhat differs from the others in the fact that, according to the data given by Stubican and Hannon [21], the logical evolution of t′ at 1200 °C is not $t' \rightarrow c + t$, but rather $t' \rightarrow c + m$: the monoclinic phase is stable for this composition up to around 1350 °C (Fig. 2). Most of the monoclinic phase observed at room temperature after annealing has formed at 1200 °C and not on cooling.

All in all, it is possible to propose that when such samples are annealed, it is roughly equivalent to raising the hafnia content or the annealing temperature, as far as the t′ return to equilibrium and sample microstructure is concerned. This is supported by the analysis detailed in the latter section, if one considers that raising the hafnia content and annealing temperature may have an equivalent influence on the yttrium diffusion energy. In the former case, this energy increases because t′ metastability does. In the latter, thermal activation is responsible for the increase of diffusion-specific energy.

5.3. Thermomechanical behaviour

The marked decrease of thermal cycling sample lifetimes, with increasing hafnia content, is not clearly understood. Indeed, the spallation mechanism of the hafnia-containing samples is the same as that of the classical Y-PSZ: a macrocrack propagates parallel to and near the ceramic/bondcoat interface, within the ceramic coating. This interface is therefore not the weak link for the durability of the system. At this point, one should have to consider that the mechanism which leads to the coating's failure (thermal expansion mismatch between the ceramic and the substrate) implies that the system works under imposed strains. Here, the stress level in the coating is proportional to the materials Young's modulus.

It has been shown that the Young's modulus of the yttria partially stabilized hafnia ($x = 100$) was nearly twice that of the yttria partially stabilized zirconia ($x = 0$). If one considers the fact that hafnia and zirconia-base materials have roughly the same modulus [39], this means that the ceramic droplets forming the coating are more strongly linked in hafnia-based TBC than in zirconia TBC. This could be due to the fact that the impinging hafnia-based powder grains spread upon impact with a higher kinetic energy than zirconia grains, because of their higher specific weight.

As a consequence of Young's modulus increase, the stress level would be twice as high in the case of the hafnia–yttria system under thermal cycling conditions. This result could be advanced as a first-step hypothesis to explain the observed short life in the high hafnia content samples. In addition, the evinced increase of the Young's modulus during isothermal annealing is expected to accentuate the thermal stresses and therefore accelerate coating damage. Moreover, the eventual appearance of relatively important quantities of monoclinic phase, in high hafnia content samples, associated with the corresponding volume expansion, is another prejudicial factor for the coating integrity.

Last, the fact that the number of cycles to failure is about three times higher for samples tested in "less-oxidizing conditions" than for samples tested with a 1 h dwell-time, indicates that bondcoat oxidation, as well as the return of t′ phase to equilibrium and droplets sintering leading to Young's modulus increase, account for the accumulated damage that finally leads to sample failure.

6. Conclusion

The potential of hafnia as a ceramic material to be totally or partially substituted for zirconia to form plasma-sprayed thermal barrier coatings has been investigated. It has been shown that the similarities between the ZrO_2–Y_2O_3 and HfO_2–Y_2O_3 equilibrium phase diagrams also extend to the formation of non-equilibrium phases. Yttria-partially stabilized zirconia–hafnia mixtures all exhibit upon fast quenching a single metastable t′ phase with a microstructure equivalent to that of pure YPSZ t′ phase. It has also been shown that the stability of this t′ phase at elevated temperature is highly dependent on the chemical composition of the ceramic. It is proposed that mixtures containing higher levels of hafnia exhibit a $c \rightarrow t'$ transformation at higher temperatures; the t′ phase would be, at a given temperature, all the more unstable towards diffusion. It is accordingly observed that the return of t′ to equilibrium is faster when hafnia is progressively substituted for zirconia. The Young's modulus of the as-sprayed coatings also increases monotonically with increasing hafnia content. Because the degradation mode in thermomechanical experiments is the same, whatever the hafnia content, there is a proved link between this parameter and the thermomechanical resistance of the coating.

Acknowledgements

The authors gratefully acknowledge the help of Thierry Ochin for X-ray diffraction measurements. The zirconia–hafnia powders were provided by CENG/CEREM. Bondcoat and topcoat plasma spraying was performed, respectively, by Sochata and Snecma. This work was partially funded by DRET under grant 89-34-001 BC 121.

References

1. K. D. LEVINE and R. A. MILLER, EPRI AP-2618, Electric Power Research Institute, Palo Alto CA (1982).
2. T. COSACK, L. PAWLOWSKI, S. SCHNEIDERBANGER and S. STURLESE, *Trans. ASME* (1992) 92-GT-319.
3. H. D. STEFFENS and R. KACZMAREK, *Weld. World* **28** (1990) 224.
4. R. E. DEMARAY, J. W. FAIRBANKS and D. H. BOONE, in "ASME Gas Turbine Conference", London, 1982.
5. F. C. TORIZ, A. B. THAKKER, and S. K. GUPTA, *Surf. Coatings Technol.* **39/40** (1989) 161.
6. S. STECURA, NASA Technical Memo 86905 (1985).
7. R. A. MILLER, J. L. SMIALEK and R. G. GARLICK, in "Science and Technology of Zirconia, Advances in Ceramics", Vol. 3, edited by A. H. Heuer and L. W. Hobbs (American Ceramic Society, Columbus, OH, 1981) p. 241.
8. R. A. MILLER, R. G. GARLICK and J. L. SMIALEK, *Ceram. Bull.* **62** (1983) 1355.
9. C. A. ANDERSON and T. K. GUPTA, in "Science and Technology of Zirconia, Advances in Ceramics", Vol. 3, edited by A. H. Heuer and L. W. Hobbs, (American Ceramic Society, Columbus, OH, 1981) p. 184
10. V. LANTERI, R. CHAIM and A. H. HEUER, *J. Am. Ceram. Soc.* **69** (1986) 258.
11. L. LELAIT and S. ALPERINE, *Scripta Metall. Mater.* **25** (1991) 1815.
12. S. ALPERINE and L. LELAIT, *Trans. ASME* (1992) 92-GT-317.
13. O. MULLER and R. ROY "The Major Ternary Structural Families" (Springer, New York, 1974) p. 5.
14. P. R. STASZAK, G. P. WIRTZ, M. BERG and S. D. BROWN, NASA Final Report NAG 3–495, Vol. 1 (1968) p. 29.
15. C. E. CURTIS, L. M. DONEY and J. R. JOHNSON, *J. Am. Ceram. Soc.* **37** (1954) 458.
16. M. F. TRUBELJA, PhD thesis, Pennsylvania State University, PA (1987).
17. R. RUH, H. J. GARRETT and R. F. DOMAGALA, *J. Amer. Ceram. Soc.* **51** (1968) 23.
18. J. LEFÊVRE, *Ann. Chim.* **8** (1963) 117.
19. G. M. WOLTEN, *J. Am. Ceram Soc.* **46** (1963) 418.
20. D. W. STACY and D. R. WILDER, *ibid.* **58** (1975) 285.
21. V. S. STUBICAN and R. HANNON, in "Science and Technology of Zirconia III, Advances in Ceramics" Vol. 24A, edited by S. Somiya, N. Yamamoto and H. Hanagida (American Ceramic Society, Columbus, OH, 1988) p. 71.
22. M. G. SCOTT, *J. Mater Sci.* **10** (1975) 1527.
23. H. TORAYA, Y. MASAHIRO and S. SOMIYA, *J. Am. Ceram. Soc.* **67** (1984) C119.
24. B. D. CULLITY, "Elements of X-ray Diffraction" (Addison-Wesley, USA, 1967) p. 389.
25. D. K. SMITH and H. W. NEWKIRK, *Acta Crystallogr.* **18** (1965) 983.
26. J. ADAMS and M. D. RODGERS, *ibid.* **12** (1959) 951.
27. G. TEUFER, *ibid.* **15** (1962) 1187.
28. H. TORAYA, Y. MASAHIRO and S. SOMIYA, *J. Am. Ceram. Soc.* **67** (1984) C181.
29. E. D. WHITNEY, *Trans. Farad. Soc.* **61** (1965) 1991.
30. V. LANTERI, PhD thesis, Case Western Reserve University, Cleveland, OH (1986).
31. L. LELAIT, Thèse, Université d'Orsay, France (1991).
32. T. SAKUMA, Y. YOSHIZAWA and H. SUTO, *J. Mater. Sci.* **20** (1985) 1085.
33. R. MEVREL, *Mater. Sci. Eng. (A)* **120** (1989) 13.
34. L. LELAIT, S. ALPERINE, C. DIOT and R. MEVREL, *ibid.* **120/121** (1989) 475.
35. V. PEROVIC, G. R. PURDY and L. M. BROWN, *Acta Metall.* **27** (1978) 1075.
36. L. M. BROWN, R. H. COOK, R. K. HAM and G. R. PURDY, *Scripta Metall.* **7** (1973) 815.
37. S. WEN, A. G. KHATCHATURYAN and J. W. MORRIS, *Metall. Trans. A*, **12A** (1981) 581.
38. P. W. VOORHEES, *J. Statist. Phys.* **38** (1985) 231.
39. J. WANG, H. P. LI and R. STEVENS, *J. Mater. Sci.* **27** (1992) 5397.
40. R. RUH and P. W. R. CORFIELD, *J. Am. Ceram. Soc.* **53** (1970) 126.
41. V. B. GLUSHKOVA and M. V. KRAVCHINSKAYA, *Ceram. Int.* **11** (1985) 56.

Received 22 October 1993
and accepted 27 July 1994